FULL PAPER

Perovskites

ADVANCED
ENERGY
MATERIALS

www.advenergymat.de

Flash Infrared Annealing for Antisolvent-Free Highly Efficient Perovskite Solar Cells

Sandy Sanchez, Xiao Hua, Nga Phung, Ullrich Steiner, and Antonio Abate*

Organic–inorganic perovskites have demonstrated an impressive potential for the design of the next generation of solar cells. Perovskite solar cells (PSCs) are currently considered for scaling up and commercialization. Many of the lab-scale preparation methods are however difficult to scale up or are environmentally unfriendly. The highest efficient PSCs are currently prepared using the antisolvent method, which utilizes a significant amount of an organic solvent to induce perovskite crystallization in a thin film. An antisolvent-free method is developed in this work using flash infrared annealing (FIRA) to prepare methylammonium lead iodide (MAPbI$_3$) PSCs with a record stabilized power conversion efficiency of 18.3%. With an irradiation time of fewer than 2 s, FIRA enables the coating of glass and plastic substrates with pinhole-free perovskite films that exhibit micrometer-size crystalline domains. This work discusses the FIRA-induced crystallization mechanism and unveils the main parameters controlling the film morphology. The replacement of the antisolvent method and the larger crystalline domains resulting from flash annealing make FIRA a highly promising method for the scale-up of PSC manufacture.

1. Introduction

The recent demonstration of several organic–inorganic perovskites as photovoltaic materials opened new opportunities for low-cost solar energy conversion.[1–5] Perovskite solar cells (PSCs) currently have lab-scale power conversion efficiencies (PCE) that approach those of established inorganic technologies, such as crystalline silicon.[6] Scaling up the current PSC preparation procedures is, however, neither practical nor environmentally friendly. Indeed, one of the usually adopted and most effective lab-scale method to induce perovskite crystallization, the "antisolvent method," requires a relative amount of solvent (more than 50 µL cm^{-2}) that is typically not reclaimed.[7,8] The antisolvent method is effective because it

enables the dense and uniform coverage of perovskite films on suitable substrates, which is a key requirement to achieve highly efficient PSCs.[9] It works on small areas (several square centimeters, i.e., for lab-scale devices), but is difficult to apply on larger surfaces, causing practical issues for PSC scale-up and commercialization.

Several antisolvent-free methods have been proposed to control perovskite film crystallization, resulting in PSCs with relatively high PCEs.[10–14] For example, Nie et al. demonstrated a hot-casting technique to grow continuous, pinhole-free perovskite films with millimeter-scale crystalline grains.[8] This method uses a hot (≈70 °C) solution of lead iodide and methylamine hydrochloride spin-coated onto a hot (180 °C) substrate. This technique allowed the fabrication of planar solar cells with average (not stabilized) efficiencies approaching 16%. Li et al. proposed a vacuum-assisted method for 1 cm^2 PSCs with a stabilized PCE of around 20%.[9] Nevertheless, the extension of PSCs toward a technology remains challenging because of the lack of a method allowing to produce large-area devices (100 cm^2 or larger) with PCEs comparable to lab-scale devices.

Rapid thermal annealing methods have been successfully used to control the crystallization of inorganic semiconductors and to prepare large-area devices made of highly crystalline phase-continuous films.[15,16] Similar approaches have been explored for PSCs with promising results.[17–20] In this direction, Troughton et al. proposed a short exposure to a highly intense near-infrared radiation to crystallize perovskite films, potentially enabling the preparation of large-area PSCs with high efficiencies.[18] This report was the first to introduce the flash infrared annealing (FIRA) as a method to synthesize perovskite films. In this study, however, infrared-absorbing Al$_2$O$_3$ nanoparticles were added to the perovskite, which may interfere with homogeneous film formation and perovskite crystallization.

In this work, we demonstrate FIRA, an antisolvent-free method that can be used to prepare methylammonium lead iodide (MAPbI$_3$) PSCs with stabilized power conversion efficiencies up to 18.3%. In particular, our method does not rely on the addition of IR absorber to the perovskite film. The perovskite film crystallization is completed within 2 s followed by 8 s in the dark at low temperatures in the FIRA oven to remove the solvent from the film completely (see Figures S1 and S2, Supporting Information). During this process, rapid crystallization

S. Sanchez, Dr. X. Hua, Prof. U. Steiner
Adolphe Merkle Institute
University of Fribourg
Chemin des Verdiers 4, CH-1700 Fribourg, Switzerland
N. Phung, Dr. A. Abate
Helmholtz-Zentrum Berlin für Materialien und Energie
Kekuléstrasse 5, 12489 Berlin, Germany
E-mail: antonio.abate@helmholtz-berlin.de

The ORCID identification number(s) for the author(s) of this article can be found under https://doi.org/10.1002/aenm.201702915.

**ADVANCED
SCIENCE NEWS**

www.advancedsciencenews.com

**ADVANCED
ENERGY
MATERIALS**

www.advenergymat.de

results in micrometer-size crystal grains arranged in a dense perovskite film. We discuss the key parameters that control perovskite film crystallization allowing the manufacture of devices with PCEs comparable to those made with the antisolvent method. We show that FIRA allows the manufacture of large-area perovskite films (100 cm^2) and large-area devices (1.4 cm^2 of active area). Note that FIRA does not significantly heat the substrate and is thus compatible with low-temperature processing on plastic substrates, enabling in particular roll-to-roll printing.

2. Perovskite Film Crystallization

Crystallization from a solution typically occurs by self-seeding and in **Figure 1** is showed a concentration scheme and temperature profile as a function of the time to form a solid from solution. Figure 1a schematically shows a typical concentration profile (LaMer curve), where the solution is concentrated above the solubility limit C_s. Self-seeding is induced upon surpassing a certain critical concentration value C_c, which should

lie below the maximal supersaturation C_m, above which the substance (i.e., the perovskite) precipitates in an uncontrolled fashion. In stage 1 up to a time limit t_1, the solution concentration is increased by solvent evaporation. This is followed by stage 2 until time t_2, where crystal nuclei form by self-seeding. Crystal nucleation and growth remove the crystallizing substance from the solution, thereby reducing the concentration. This, in turn, reduces the nucleation of further crystals. The interplay of further solvent removal and crystal growth often results in a steady-state concentration that lies between C_s and C_c, as indicated in stage 3 from time t_2 to t_3.[21,22] The nucleation rate is predominantly influenced by the depth of the quench in stage 2, that is, the maximum concentration reached in Figure 1a. High nucleation rates arise from a supersaturation, which is caused by a rapid variation of the concentration.[23–25] In the antisolvent method, rather than removing the solvent as described above, high supersaturation-induced nucleation is caused by a change in C_s, C_c, and C_m by the addition of a poor solvent for the perovskite.

Within the framework of Figure 1a, the state-of-the-art antisolvent method induces a high nucleation density by the abrupt reduction of the solubility of the perovskite precursors in solution, resulting in a high nucleation density followed by crystal growth, providing a laterally continuous perovskite crystal morphology.[26–28] In a more general approach, crystal nucleation from solution proceeds by supersaturating the solution, which can be achieved by solvent evaporation.[29–31] Pascoe et al. illustrated that through the manipulation of the solution concentration and degree of supersaturation, it is possible to vary the spacing between nucleation sites from a few hundred nanometers to a few hundred micrometers.[32] They highlight the importance of the rate of heterogeneous nucleation to grow up to a final compact film, which was achieved by controlling the solvent evaporation rate through a variation of the nitrogen flow rate across the drying film.

Concentrating the perovskite solution through solvent evaporation by heating, however, faces the challenge of maintaining the temperature of the perovskite film below its degradation temperature, while preventing the dewetting of the film. FIRA allows very rapid film formation and perovskite crystallization. Very short heath pulses substantially reduce the degradation of organic materials even at very high temperatures, as has been demonstrated in polymer films.[5,33] The rapid solvent removal afforded by FIRA affords the control of perovskite film formation and crystallization, see **Figure 2**, avoiding the detrimental effects of dewetting and perovskite degradation.

Figure 1b shows the surface temperature of a perovskite film (acquired by an IR camera), the surface temperature of the FTO (measured by a wire thermocouple) and the temperature of the FIRA internal chamber (measured by a K-type thermocouple) as a function of time, during and 2 s after the IR flash. In particular, the perovskite surface temperature indicates a crystallization process at quite low temperatures (70 °C peak). This is advantageous and consistent with recent studies, showing the relationship between low-temperature perovskite crystal growth (below 100 °C) and the improvement of the structural and optoelectronic properties of PSCs.[34,21] Nevertheless, because the FTO layer is a high IR absorber, the temperature above its surface reaches 480 °C after 2 s of IR exposure (Figure 1b),
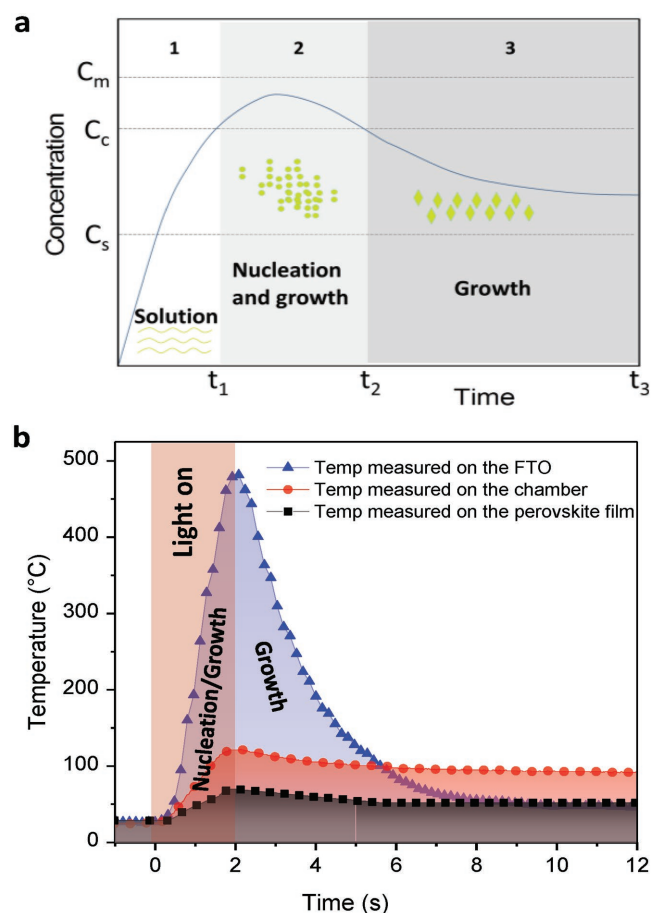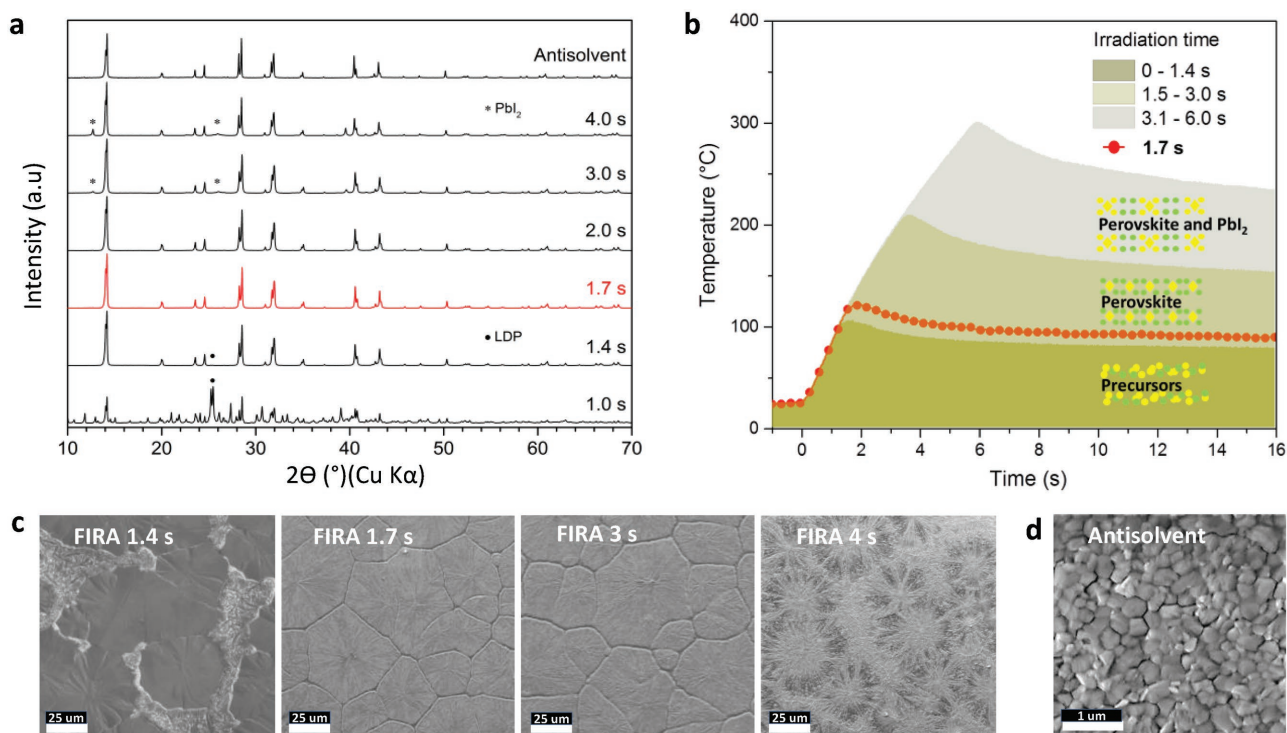

Figure 1. Nucleation and growth dynamics and temperature measured during flash annealing. a) Schematic representation of the concentration variation during crystal nucleation and growth according to the LaMer curve. b) Temperature measured in the chamber and on the FTO surface with thermocouples and surface temperature of the perovskite film measured by an IR camera.

Figure 2. IR annealing time and its relation to the crystal perovskite formation. a) XRD pattern of selected devices, where the black circles and asterisks mark the main reflections of the lower dimensional perovskite (LDP) and PbI_2, respectively. b) Temperature profiles as measured from the thermocouple close to the substrate for different FIRA annealing pulse lengths. c) Top view of FIRA-annealed perovskite films for four annealing times, scale bar: 25 µm. d) Top view of a reference film made by the antisolvent method followed by annealing at 100 °C for 1 h on a standard hotplate, scale bar: 1 µm.

confirming the high energy that FIRA can achieve with an IR short pulse.

Figure 2c shows that the perovskite nucleation rate during FIRA annealing is lower compared to the antisolvent method, indicating either a lower supersaturation or a time-limitation of the nucleation phase by the shortness of the heating pulse. The resulting lower nucleation density followed by crystal growth results in larger lateral crystal domains, which is beneficial for the performance of PSCs.[35] Assuming time-limited nucleation, a control of the flash duration controls the nucleation density, while the flash power determines the energy deposited in the film, allowing crystal growth to proceed after the flash. The optimization of these two parameters enables the formation of large perovskite crystals.

2.1. Controlling Perovskite Crystallization through FIRA Pulse Duration

As described above, the perovskite pulse length is likely to control the nucleation density. The energy deposited in the film must be sufficiently large to allow the complete crystallization of the film (by crystal growth) without inducing parasitic effects (perovskite degradation).[36,37] Here, we focused on the role of the FIRA flash time on controlling the film morphology and crystallinity, keeping all other experimental parameters constant. The temperature in the chamber was used to measure different annealing times, and the samples were kept in the FIRA chamber for eight additional seconds after the IR irradiation, as previously stated.

X-ray diffraction (XRD, Figure 2a) was employed to investigate the crystal structure in the films as a function of the FIRA pulse duration. The XRD patterns show that all samples, apart from the 1.0 s sample, are dominated by the tetragonal ($I4/mcm$) $MAPbI_3$ perovskite phase. Although the 1.0 s sample also shows the presence of the $MAPbI_3$, it has a much larger contribution from a low-dimensional perovskite (LDP).[20] This phase has a lower symmetry, which probably stems from the incomplete crystallization of the precursor solution, that is, the inclusion of solvent within the crystal morphology.[38,39] A small amount of this phase can also be identified in the 1.4 s sample. The 1.7 and 2.0 s samples show almost identical patterns that resemble the data from the antisolvent sample (see Figure S3 and Tables S1–S3, Supporting Information, for the refined crystal structures). From 3.0 to 4.0 s, a growing contribution of PbI_2 can be observed, which we attribute to the degradation of $MAPbI_3$ caused by the long irradiation time and thus higher local temperature. Figure 2b shows the temperature profiles (measured by a thermocouple close to the substrate surface) as a function of the FIRA time, delimiting three regimes of different LDP–perovskite–PbI_2 compositions. This plot allows identifying the optimal pulse duration in the range of 1.5–3 s, enabling the formation of a phase-pure of perovskite film. The red line represents the temperature profile that yields the best device performance as described below.

Figure 2c shows top-view scanning electron microscope images of perovskite film morphologies for 4 s FIRA pulse times. All images show large crystalline domains with diameters around 40 µm. The shortest 1.4 s sample image reveals

**ADVANCED
SCIENCE NEWS**

www.advancedsciencenews.com

**ADVANCED
ENERGY
MATERIALS**

www.advenergymat.de

individual domains separated by seemingly noncrystalline regions, in good agreement with the LDP impurities of Figure 2a. 1.7 and 3 s pulse times result in large, laterally space-filling, pinhole-free crystalline domains in the films. To support it, an optical image and energy-dispersive X-ray spectroscopy (EDS) analysis of perovskite films for FIRA 1.7 s annealed are provided in Figure S4 (Supporting Information). For FIRA pulse times exceeding 4 s, the change in morphology indicates a further phase change. Supported by the XRD analysis, this is attributed to the partial degradation of the MAPbI$_3$ to PbI$_2$. In Figure 2d, the morphology of the antisolvent-manufactured film annealed for 1 h at 100 °C (according to the recipe used to prepare state-of-the-art PSCs) exhibits much smaller crystalline domains of less than 500 nm in diameter, in agreement with the published literature.[6,40] FIRA thus enables the manufacture of highly compact, pinhole-free, perovskite films with crystalline domains that are significantly larger than those produced by the antisolvent method.

3. Photovoltaic Performance

To demonstrate that devices made with FIRA-annealed perovskite layers are as efficient as those made using the state-of-the-art method, these two types of PSCs are compared in **Figure 3**. Figure 3a shows SEM cross-sectional images of complete PSCs prepared using the two methods. The FIRA-annealed perovskite

film is around 700–800 nm thick, compared to ≈500 nm for the reference PSC (made by using the antisolvent method). The current density–voltage (J–V) curves and the corresponding device performance parameters for the two champion cells are shown in Figure 3b. The FIRA-annealed PSCs exhibit a slightly higher fill factor (FF) and lower open-circuit voltage (V_{oc}) than the champion device made using the antisolvent method, while the short-circuit currents (J_{sc}) are similar. External quantum efficiency (EQE) has been collected to validate the PV parameters of the FIRA devices (see Figure S5, Supporting Information) confirming a high J_{sc} of 20.9 mA cm^{-2}. Note that the current density of the FIRA device decreases between short-circuit condition and 0.6 V forward bias, while it stays constant in the reference champion device. This is probably due to the fact the perovskite film is slightly too thick in the FIRA device, compared to the ideal thickness ≈500 nm as optimized for the antisolvent method. This results in a slightly higher series resistance, the absence of which would enhance the fill factor even more. Intensity modulated photocurrent spectroscopy analysis is provided and discussed in the Supporting Information (Figure S6, Supporting Information) to support these arguments.

Figure 3c displays the statistical analysis of the performance parameters collected from 20 devices, which confirm the trend observed for the champion devices. Finally, the maximum power output stabilized for 5 min in Figure 3d shows that the champion FIRA device stabilized PCE performance of ≈18.3%
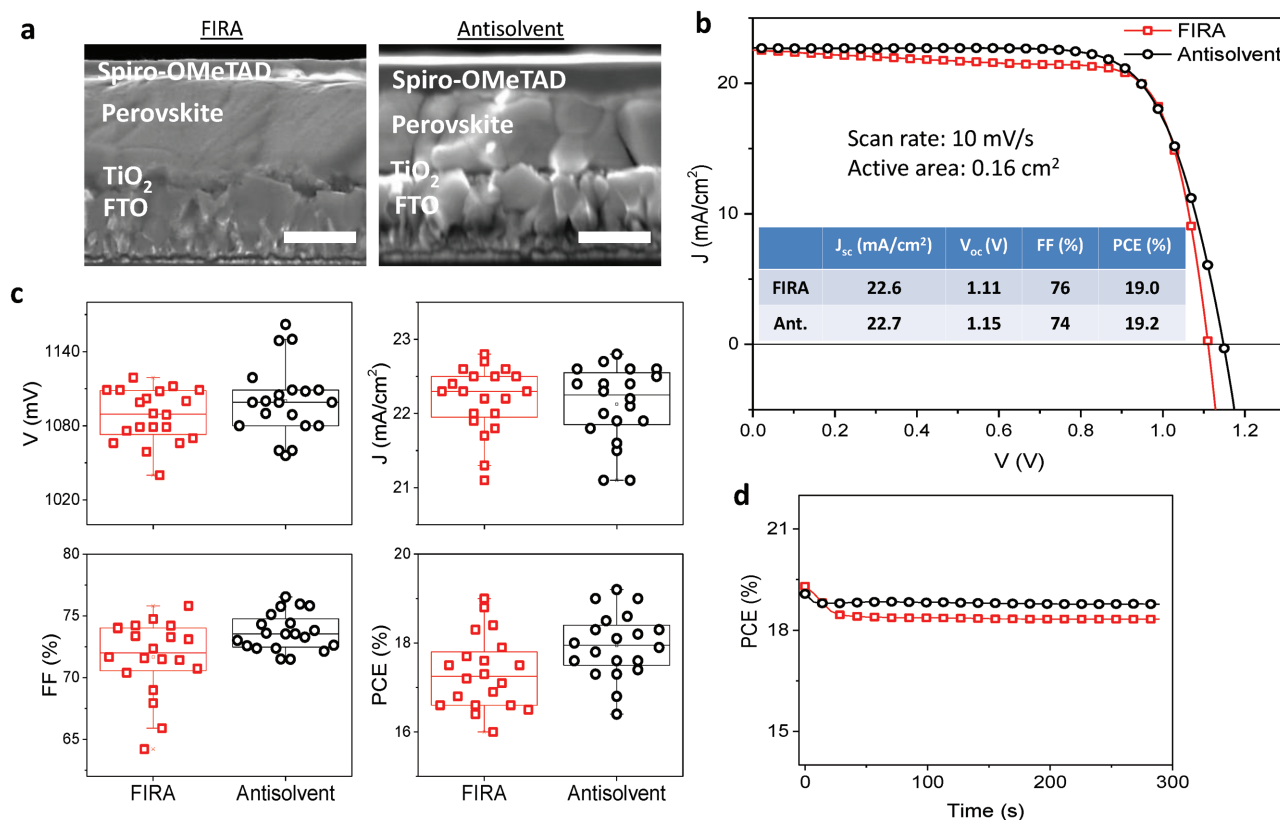

Figure 3. a) SEM cross-sectional images of complete PSCs, scale bar: 500 nm. b) Current density–voltage (J–V) scans collected at 10 mV s^{-1} of two champion devices under 1.5 AM irradiation and the corresponding photovoltaic performance parameters. c) J_{sc}, V_{oc}, FF, and PCE statistics for 20 devices. d) Maximum power point tracking of the champion cells (error: ±0.2 PCE).

**ADVANCED
SCIENCE NEWS**

www.advancedsciencenews.com

**ADVANCED
ENERGY
MATERIALS**

www.advenergymat.de

is comparable to that of the reference, which is among the highest values reported for MAPbI₃ based PSCs made by rapid thermal annealing. A long-term stability study was carried out with the FIRA and antisolvent devices by light exposition (1 sun) during one week under a nitrogen atmosphere. The result of this study (Figure S7 and Table S4, Supporting Information) shows stable PSCs made by FIRA and antisolvent method, where the maximum PCE loss did not exceed 4% of the total initial PCE.

4. FIRA as a Method to Scale up the Manufacture of Perovskite Solar Cells

Foreseeing the commercialization of PSCs, **Figure 4** shows large-area perovskite synthesis employing FIRA to crystallize the film. The perovskite precursor solution can be deposited on the substrate using any of the roll-to-roll compatible methods available on the market, such as doctor-blading, slot-casting, spray-coating, screen-printing, and inject-printing.[41] The deposited film is then passed through the FIRA box, which enables rapid (within 2 s) perovskite film crystallization (see the Experimental Section for details).

Figure 4a shows the surface temperature of a perovskite film measured by an IR camera during heating. It shows that the IR radiation is mainly absorbed in the FTO layer, which then heats the perovskite solution film to initiate the crystallization, while the substrate stays close to room temperature (Figure S2, Supporting Information). This result indicates that FIRA is compatible with the use of polymeric substrates, further enhancing its use in a roll-to-roll manufacturing process. Preliminary tests on manufacturing uniform large-area perovskite films (100 cm²) are shown in Figure 4b, both for glass and polymeric (PET) substrates. To prove FIRA potential for manufacturing large-area PSCs, we prepared and tested devices with 1.4 cm² of the active area (lab-scale devices have an active area of 0.1 cm² about). Figure 4c shows the J–V curve for a champion large-area device with 14.6% of PCE, achieving a V_{oc} of more than 1 V. We note that the FF is significantly lower than in lab-scale devices (Figure 3), which is most likely due to a limiting series resistance introduced by the larger device active area.[42,43]
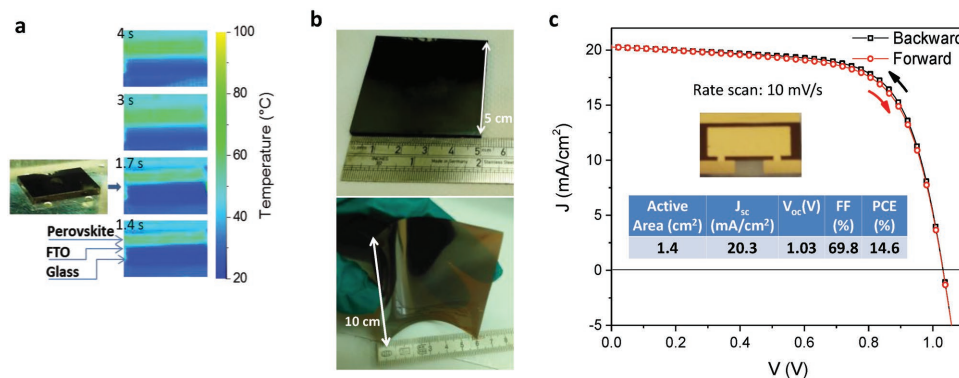
5. Conclusion

We demonstrate FIRA as a new method to prepare state-of-the-art efficiency perovskite solar cells with a good reproducibility. The advantages of FIRA are: (i) the elimination of the antisolvent to induce the perovskite film crystallization, which drastically reduces the use of organic solvent in the PSC manufacture, making the process environmental friendlier; (ii) FIRA is compatible with large-area device manufacture and flexible substrates which require low-temperature processing; (iii) FIRA is suitable for fast throughput production lines, such as roll-to-roll deposition methods. We foresee FIRA as one of the most promising methods to scale up perovskite solar cells on flexible substrates.

6. Experimental Section

Method: Photovoltaic devices were fabricated on FTO-coated glass (Pilkington NSG TEC). The substrates were cleaned with Hellmanex soap, followed by 30 min sonication in a Hellmanex 2% water solution, 15 min sonication in IPA, and 5 min of oxygen plasma etching. Then, 30 nm thick TiO₂ compact layers were deposited onto the FTO by spray pyrolysis at 450 °C from a precursor solution of titanium diisopropoxide bis(acetylacetonate) in anhydrous ethanol and acetylacetonate. After the spraying, the FTO substrates were left at 450 °C for 5 min before cooling to room temperature. Then, a mesoporous TiO₂ layer was deposited by spin-coating for 10 s at 4000 rpm with a ramp of 2000 rpm s⁻¹, using a 30 nm particle paste (Dyesol 30 NR-D) diluted in ethanol to achieve 150–200 nm thick layers. After the spin-coating, the FTO substrates were dried at 100 °C for 10 min, and the films were annealed on a programmable hotplate (2000 W, Harry Gestigkeit GmbH) to crystallize TiO₂ at 450 °C for 30 min under dry air flow. Li-doping of the mesoporous TiO₂, as described elsewhere, was accomplished by spin-coating a 0.1 M solution of bis(trifluoromethane)sulfonimide lithium salt (Li-TFSI) in acetonitrile at 3000 rpm for 10 s followed by another sintering step at 450 °C for 30 min.[34] After cooling down to 150 °C, all the substrates were immediately transferred in a nitrogen atmosphere glovebox (with an overpressure varying of 2–3 mbar) for the deposition of the perovskite films.

Perovskite Precursor Solutions and Film Preparation: The organic salts were purchased from Dyesol; the lead compounds from TCI. The MAPbI₃ perovskite precursor solution contained MAI (1 M), PbI₂ 1 M in anhydrous 3 v/v DMF:1 v/v DMSO. The perovskite control films were deposited as previously reported.[1,44] The perovskite solution was spin-coated in two

Figure 4. a) Temperature variation of a perovskite film supported on an FTO–glass substrate, measured in situ with an IR camera. b) Pictures of large perovskite films made by FIRA on FTO-coated glass and ITO-coated PET (flexible) substrates. c) Current density–voltage scans collected at 10 mV s⁻¹ of the champion large-area device under 1.5 AM irradiation and the corresponding photovoltaic performance parameters. Inset: a picture of the device with 1.4 cm² active area.

steps at 1000 and 6000 rpm for 10 and 20 s, respectively. During the second step, 100 μL of chlorobenzene was poured onto the spinning substrate 5 s before the end of the program. The substrates were then annealed at 100 °C for 1 h in a nitrogen-filled glovebox. After perovskite annealing, the substrates were cooled down within a few minutes. The films made by the FIRA include the spin-coating of the perovskite solution in a single step at 4000 rpm for 10 s. The substrates were then IR irradiated for 1.7 s in the FIRA oven and were kept there for ten additional seconds before removal and cooling within several minutes. The FIRA processing was carried out in a standard fume hood. One of the most important parameters is the relative humidity during manufacture, which may well be the fundamental reason for the performance difference in between antisolvent and FIRA devices. The FIRA devices are made in a fume hood with ≈30% relative humidity, which is a drawback that must be addressed to achieve the highest performances.

Immediately after cooling the perovskite films, a spiro-OMeTAD (Merck) solution (70×10^{-3} M in chlorobenzene) was deposited by spin-coating at 4000 rpm for 20 s. Spiro-OMeTAD was doped with Li-TFSI (Sigma Aldrich), tris(2-(1H-pyrazol-1-yl)-4-tert-butylpyridine)-cobalt(III) tris(bis(trifluoromethylsulfonyl)imide) (FK209, Dynamo), and 4-tert-butylpyridine (TBP, Sigma-Aldrich). The molar ratio of the additives to spiro-OMeTAD was: 0.5, 0.03, and 3.3 for Li-TFSI, FK209, and TBP, respectively. Finally, an 80 nm thick gold top-electrode was thermally evaporated under high vacuum.

Photovoltaic Device Testing: For photovoltaic measurements, a solar simulator from ABET Technologies (Model 11016 Sun 2000) with a xenon arc lamp was used, and the solar cell response was recorded using a Metrohm PGSTAT302N Autolab. The intensity of the solar simulator was calibrated to 100 mW cm^{-2} using a silicon reference cell from ReRa Solutions (KG5 filtered). J–V curves were measured in reverse and forward bias at a scan rate of 10 mV s^{-1}; this slow scan rate was used in all J–V measurements to minimize hysteresis effects. A shadow mask was used to define the active device area with 0.16 cm^2 of aperture and for those devices called "large area," the aperture corresponds to 1.4 cm^2. Maximum power point tracking was used to perform stability experiments. IMPS was performed according to the procedure described in the literature, using a 625 nm LED driver at short-circuit conditions and a light intensity of 100 mW cm^{-2} and a Metrohm PGSTAT302N Autolab. The EQE setup used was integrated inside the glovebox with an inert atmosphere (fill with nitrogen) including an Oriel Instruments QEPVSI-b system, a Xenon arc lamp Newport 300 W, a chopper (put at 35.5 Hz), and Newport Cornerstone 260 monochromatic. A silicon diode was used to calibrate the lamp to subtract the background light noise. The monochromatic light spot was controlled such that the spot fit inside the active area of the device and the sample was ≈1.05 mm away from the light source. EQE measurement was carried out at short-circuit current.

Temperature Measurement: The temperature in the chamber was measured using a K-type thermocouple and for the surface temperature of the FTO was used a wire J-type thermocouple, both connected to an Analogue Devices AD595 amplifier interfaced with LabView software. The surface temperature of the perovskite film was measured in situ by a FLIR T62101 IR Video Camera.

Material Characterization: Scanning electron microscopy and energy dispersive X-ray spectroscopy were carried out on a Tescan MIRA 3 LMH with a field emission source operated at an acceleration voltage of 10 kV using an octane-pro EDS detector. Powder X-ray diffraction was performed in a transmission geometry with Cu target (λ = 1.5401 Å) using a STOE STADI P diffractometer. Powder samples were carefully scraped off the substrates right after the annealing was finished. The transmission was imaged using a Zeiss Axio-Scope A1 Pol using a Zeiss EC Epiplan-Apochromat 20× objective.

Supporting Information

Supporting Information is available from the Wiley Online Library or from the author.

[1] J. M. Ball, M. M. Lee, A. Hey, H. J. Snaith, *Energy Environ. Sci.* **2013**, 6, 1739.

[2] H.-S. Kim, C.-R. Lee, J.-H. Im, K.-B. Lee, T. Moehl, A. Marchioro, S.-J. Moon, R. Humphry-Baker, J.-H. Yum, J. E. Moser, M. Grätzel, N.-G. Park, *Sci. Rep.* **2012**, 2, 591.

[3] J.-H. Im, C.-R. Lee, J.-W. Lee, S.-W. Park, N.-G. Park, *Nanoscale* **2011**, 3, 4088.

[4] M. M. Lee, J. Teuscher, T. Miyasaka, T. N. Murakami, H. J. Snaith, *Science* **2012**, 338, 643.

[5] J.-S. Chen, C. K. Ober, M. D. Poliks, Y. Zhang, U. Wiesner, C. Cohen, *Polymer* **2004**, 45, 1939.

[6] M. Saliba, T. Matsui, K. Domanski, J.-Y. Seo, A. Ummadisingu, S. M. Zakeeruddin, J.-P. Correa-Baena, W. R. Tress, A. Abate, A. Hagfeldt, M. Grätzel, *Science* **2016**, 354, 206.

[7] M. Li, X. Yan, Z. Kang, Y. Liao, Y. Li, X. Zheng, P. Lin, J. Meng, Y. Zhang, *ACS Appl. Mater. Interfaces* **2017**, 9, 7224.

[8] X. Zheng, B. Chen, C. Wu, S. Priya, *Nano Energy* **2015**, 17, 269.

[9] Y. Yu, S. Yang, L. Lei, Q. Cao, J. Shao, S. Zhang, Y. Liu, *ACS Appl. Mater. Interfaces* **2017**, 9, 3667.

[10] W. Nie, H. Tsai, R. Asadpour, J.-C. Blancon, A. J. Neukirch, G. Gupta, J. J. Crochet, M. Chhowalla, S. Tretiak, M. A. Alam, H.-L. Wang, A. D. Mohite, *Science* **2015**, 347, 522.

[11] X. Li, D. Bi, C. Yi, J.-D. Décoppet, J. Luo, S. M. Zakeeruddin, A. Hagfeldt, M. Grätzel, *Science* **2016**, 353, 58.

[12] G.-J. Yang, B. Ding, Y. Li, S.-Y. Huang, Q.-Q. Chu, C. Li, C. Li, *J. Mater. Chem. A* **2017**, 5, 6840.

[13] H. Wang, J. Lei, F. Gao, Z. Yang, D. Yang, J. Jiang, J. Li, X. Hu, X. Ren, B. Liu, J. Liu, H. Lei, Z. Liu, S. Liu, *ACS Appl. Mater. Interfaces* **2017**, 9, 21756.

[14] N. K. Noel, S. N. Habisreutinger, B. Wenger, M. T. Klug, M. T. Horantner, M. B. Johnston, R. J. Nicholas, D. T. Moore, H. J. Snaith, *Energy Environ. Sci.* **2017**, 10, 145.

[15] N. Kazuo, A. Michio, W. Naozo, *Jpn. J. Appl. Phys.* **1980**, 19, L563.

[16] M. L. Terry, A. Straub, D. Inns, D. Song, A. G. Aberle, *Appl. Phys. Lett.* **2005**, 86, 172108.

[17] J. Xu, Z. Hu, X. Jia, L. Huang, X. Huang, L. Wang, P. Wang, H. Zhang, J. Zhang, J. Zhang, Y. Zhu, *Org. Electron.* **2016**, 34, 84.

[18] J. Troughton, M. J. Carnie, M. L. Davies, C. Charbonneau, E. H. Jewell, D. A. Worsley, T. M. Watson, *J. Mater. Chem. A* **2016**, 4, 3471.

[19] J. Ye, H. Zheng, L. Zhu, X. Zhang, L. Jiang, W. Chen, G. Liu, X. Pan, S. Dai, *Sol. Energy Mater. Sol. Cells* **2017**, 160, 60.

[20] J. Troughton, C. Charbonneau, M. J. Carnie, M. L. Davies, D. A. Worsley, T. M. Watson, *J. Mater. Chem. A* **2015**, *3*, 9123.

[21] C. Aranda, C. Cristobal, L. Shooshtari, C. Li, S. Huttner, A. Guerrero, *Sustainable Energy Fuels* **2017**, *1*, 540.

[22] L.-L. Gao, K.-J. Zhang, N. Chen, G.-J. Yang, *J. Mater. Chem. A* **2017**, *5*, 18120.

[23] C. Roldan-Carmona, P. Gratia, I. Zimmermann, G. Grancini, P. Gao, M. Graetzel, M. K. Nazeeruddin, *Energy Environ. Sci.* **2015**, *8*, 3550.

[24] M. Xiao, F. Huang, W. Huang, Y. Dkhissi, Y. Zhu, J. Etheridge, A. Gray-Weale, U. Bach, Y.-B. Cheng, L. Spiccia, *Angew. Chem.* **2014**, *126*, 10056.

[25] W. S. Yang, J. H. Noh, N. J. Jeon, Y. C. Kim, S. Ryu, J. Seo, S. I. Seok, *Science* **2015**, *348*, 1234.

[26] D. Bi, C. Yi, J. Luo, J.-D. Décoppet, F. Zhang, S. M. Zakeeruddin, X. Li, A. Hagfeldt, M. Grätzel, *Nat. Energy.* **2016**, *1*, 16142.

[27] A. Cacciuto, S. Auer, D. Frenkel, *Nature* **2004**, *428*, 404.

[28] Q. Hu, L. Zhao, J. Wu, K. Gao, D. Luo, Y. Jiang, Z. Zhang, C. Zhu, E. Schaible, A. Hexemer, C. Wang, Y. Liu, W. Zhang, M. Grätzel, F. Liu, T. P. Russell, R. Zhu, Q. Gong, *Nat. Commun.* **2017**, *8*, 15688.

[29] V. K. LaMer, R. H. Dinegar, *J. Am. Chem. Soc.* **1950**, *72*, 4847.

[30] N. Sakai, Z. Wang, V. M. Burlakov, J. Lim, D. McMeekin, S. Pathak, H. J. Snaith, *Small* **2017**, *13*, 1602808.

[31] P.-W. Liang, C.-Y. Liao, C.-C. Chueh, F. Zuo, S. T. Williams, X.-K. Xin, J. Lin, A. K. Y. Jen, *Adv. Mater.* **2014**, *26*, 3748.

[32] A. R. Pascoe, Q. Gu, M. U. Rothmann, W. Li, Y. Zhang, A. D. Scully, X. Lin, L. Spiccia, U. Bach, Y.-B. Cheng, *Sci. China Mater.* **2017**, *60*, 617.

[33] J. Lee, M. C. Orilall, S. C. Warren, M. Kamperman, F. J. DiSalvo, U. Wiesner, *Nat. Mater.* **2008**, *7*, 222.

[34] J. W. Mullin, *Organic Process Research & Development*, Butterworth Heinemann, Oxford, UK **2002**, pp. 201–202.

[35] F. Huang, Y. Dkhissi, W. Huang, M. Xiao, I. Benesperi, S. Rubanov, Y. Zhu, X. Lin, L. Jiang, Y. Zhou, A. Gray-Weale, J. Etheridge, C. R. McNeill, R. A. Caruso, U. Bach, L. Spiccia, Y.-B. Cheng, *Nano Energy* **2014**, *10*, 10.

[36] X. Fang, Y. Wu, Y. Lu, Y. Sun, S. Zhang, J. Zhang, W. Zhang, N. Yuan, J. Ding, *J. Mater. Chem. C* **2017**, *5*, 842.

[37] P. K. Nayak, D. T. Moore, B. Wenger, S. Nayak, A. A. Haghighirad, A. Fineberg, N. K. Noel, O. G. Reid, G. Rumbles, P. Kukura, K. A. Vincent, H. J. Snaith, *Nat. Commun.* **2016**, *7*, 13303.

[38] Z. Song, S. C. Watthage, A. B. Phillips, B. L. Tompkins, R. J. Ellingson, M. J. Heben, *Chem. Mater.* **2015**, *27*, 4612.

[39] F. Hao, C. C. Stoumpos, Z. Liu, R. P. H. Chang, M. G. Kanatzidis, *J. Am. Chem. Soc.* **2014**, *136*, 16411.

[40] G. E. Eperon, V. M. Burlakov, P. Docampo, A. Goriely, H. J. Snaith, *Adv. Funct. Mater.* **2014**, *24*, 151.

[41] K. Hwang, Y.-S. Jung, Y.-J. Heo, F. H. Scholes, S. E. Watkins, J. Subbiah, D. J. Jones, D.-Y. Kim, D. Vak, *Adv. Mater.* **2015**, *27*, 1241.

[42] J. Lee, H. Kang, G. Kim, H. Back, J. Kim, S. Hong, B. Park, E. Lee, K. Lee, *Adv. Mater.* **2017**, *29*, 1606363.

[43] W. Chen, Y. Wu, Y. Yue, J. Liu, W. Zhang, X. Yang, H. Chen, E. Bi, I. Ashraful, M. Grätzel, L. Han, *Science* **2015**, *350*, 944.

[44] H. J. Snaith, A. Abate, J. M. Ball, G. E. Eperon, T. Leijtens, N. K. Noel, S. D. Stranks, J. T.-W. Wang, K. Wojciechowski, W. Zhang, *J. Phys. Chem. Lett.* **2014**, *5*, 1511.